

# Three-dimensional measurement of the Hanbury Brown Twiss effect for degenerate and non-degenerate bosonic ensembles

M. Schellekens,<sup>1</sup> R. Hoppeler,<sup>1</sup> A. Perrin,<sup>1</sup> J. Viana Gomes,<sup>1,2</sup>  
D. Boiron,<sup>1</sup> A. Aspect,<sup>1</sup> C. I. Westbrook<sup>1\*</sup>

<sup>1</sup>Laboratoire Charles Fabry de l’Institut d’Optique, UMR 8501 du CNRS  
Centre Scientifique d’Orsay, Bat. 503, 91403 Orsay CEDEX France

<sup>2</sup>Departamento de Fisica, Universidade do Minho  
4710-057, Braga Portugal

\*To whom correspondence should be addressed. E-mail: christoph.westbrook@iota.u-psud.fr.

**We have studied 2-body correlations of atoms in an expanding cloud above and below the Bose-Einstein condensation threshold. The observed correlation function for a thermal cloud shows a bunching behavior, while the correlation is flat for a coherent sample. These quantum correlations are the atomic analogue of the Hanbury Brown Twiss effect. We observe the effect in three dimensions and study its dependence on cloud size.**

Nearly half a century ago, Hanbury Brown and Twiss (HBT) performed a landmark experiment on light from a gaseous discharge (*I*). The experiment demonstrated strong correlations in the intensity fluctuations at two nearby points in space despite the random or chaotic nature of the source. Although the effect was easily understood in the context of classical statistical wave optics, the result was surprising when viewed in terms of the quantum theory. It implied that

photons coming from widely separated points in a source such as a star were "bunched". On the other hand, photons in a laser were not bunched (2, 3). The quest to understand the observations stimulated the birth of modern quantum optics (4). The HBT effect has since found applications in many other fields from particle physics (5) to fluid dynamics (6).

Atom or photon bunching can be understood as a two particle interference effect (7). Experimentally, one measures the joint probability for two particles, emitted from two separated source points  $A$  and  $B$ , to be detected at two detection points,  $C$  and  $D$ . One must consider the quantum mechanical amplitude for the process ( $A \rightarrow C$  and  $B \rightarrow D$ ) as well as that for ( $A \rightarrow D$  and  $B \rightarrow C$ ). If the two processes are indistinguishable, the amplitudes interfere. For bosons, the interference is constructive resulting in a joint detection probability which is enhanced compared to that of two statistically independent detection events, while for fermions the joint probability is lowered. As the detector separation is increased, the phase difference between the two amplitudes grows large enough to render the paths distinguishable and one recovers the situation for uncorrelated particles. This fact was used by HBT to measure the angular size of a star (8), but another major consequence of the observation was to draw attention to interference of two photon amplitudes which must not be confused with classical electromagnetic field amplitudes (3), and which has led to striking examples of "quantum weirdness" (9). In a laser, all photons are in the same quantum state. Hence there is only one physical process and no bunching effect. A similar effect is expected for atoms in a Bose-Einstein Condensate (BEC).

Two particle correlations have been observed both for cold neutral atoms (10, 11, 12) and for electrons (13, 14, 15), and three-particle correlations (16, 17, 18) at zero distance have also been used to study atomic gases. But the full three dimensional effect and its dependence on the size and degeneracy of a sample has yet to be demonstrated for massive particles. Here we demonstrate the effect for a cloud of atoms close to the BEC transition temperature using a

detector capable of individual particle detection. We extract, for different cloud temperatures, a three-dimensional picture of the correlations between identical particles produced by quantum interference. We also show that a BEC shows no such correlations. The results are in agreement with an ideal gas model and show the power of single particle detection techniques applied to the study of degenerate quantum gases.

The calculation of the phase difference of the possible two-particle detection amplitudes given in (7) can be adapted to the case of particles of mass  $m$  travelling to a detector in a time  $t$ . One can show that the correlation length observed at the detectors, i.e. the typical detector separation at which the relevant processes remain indistinguishable, is  $l_i = \frac{\hbar t}{ms_i}$  where  $s_i$  is the source size along the direction  $i$ ,  $\hbar$  is the reduced Planck's constant and we have assumed that the particles have propagated to the "far field" ( $l_i \gg s_i$ ). Our measurements are performed on a cloud of atoms released suddenly from a magnetic trap. As a result of the pulsed nature of the experiment, the 3 dimensions can all be treated equivalently and the relation above applies in all three. Since the trap is anisotropic, the correlation function is as well. Our sample is a magnetically trapped cloud of metastable helium atoms evaporatively cooled close to the BEC transition temperature (19). Our source is thus very small and together with a long time of flight (308 ms) and helium's small mass, we achieve large correlation volume ( $30 \times 800 \times 800 \mu\text{m}^3$ ) which simplifies the detection problem. The high phase space density of the sample also yields a high data rate for pair detection compared to many other experiments.

To detect the atoms we use an 8 cm diameter microchannel plate detector (MCP). It is placed 47 cm below the center of the magnetic trap. A delay line anode permits position sensitive detection of individual particles in the plane of the detector (20). The apparatus is shown schematically in Figure 1. Atoms are released from the trap by suddenly turning off the magnetic field. Approximately 10% of these atoms are transferred to the magnetic field insensitive  $m = 0$  state and fall freely to the detector. The remaining atoms are removed by applying

magnetic field gradients. For each detected atom we record the in-plane coordinates  $x$ ,  $y$  and the time of detection  $t$ . The atoms hit the detector at 3 m/s with little velocity spread and so we convert  $t$  into a vertical position  $z$ . The observed rms resolution is  $d \sim 250 \mu\text{m}$  in  $x$  and  $y$  and 2 nm in  $z$ . These data allow us to construct a 3 dimensional histogram of pair separations ( $\Delta x$ ,  $\Delta y$ ,  $\Delta z$ ) for all particles detected in a single cloud. The histograms are summed over the entire atomic distribution and over many shots, typically 1000 (see Materials and Methods).

Because of our excellent resolution along  $z$ , we begin by concentrating on the correlation function along this axis. Normalized correlation functions for various experimental conditions are shown in Figure 2a. To compute the normalized correlation function, we divide the pair separation histogram by the auto-convolution of the average single particle distribution along  $z$ . We also normalize the correlation function to unity for large time separations. This amounts to dividing, for each elementary pixel of our detector, the joint detection probability by the product of the individual detection probabilities at the two pixels. This gives us the usual normalized correlation function  $g^{(2)}(\Delta x = 0, \Delta y = 0, \Delta z)$ . The HBT bunching effect corresponds to the bump in the top 3 graphs of Figure 2a. The fourth graph shows the result for a BEC. No correlation is observed. (A detector saturation effect in the BEC data required a modified analysis procedure, see Materials and Methods.)

To give a full 3D-image of the correlation function, we plot in Figure 2b the normalized correlation functions in the  $\Delta x - \Delta y$  plane and for  $\Delta z = 0$ , for the same three data sets. The data in Figure 2b clearly show the asymmetry in the correlation function arising from the difference in the two transverse dimensions of the trapped cloud. The long axis of the correlation function is orthogonal to that of the magnetic trap.

We expect the experimental normalized correlation function for a thermal bosonic gas to be described by:

$$g_{th}^{(2)}(\Delta x, \Delta y, \Delta z) = 1 + \eta \exp \left( - \left[ \left( \frac{\Delta x}{l_x} \right)^2 + \left( \frac{\Delta y}{l_y} \right)^2 + \left( \frac{\Delta z}{l_z} \right)^2 \right] \right) \quad (1)$$

We have assumed here that the gas is non interacting and that the velocity distribution remains roughly Gaussian even close to the BEC transition temperature. Numerical simulations indicate that this is a good approximation when the correlation function is averaged over the entire cloud (21). As discussed above, the correlation lengths should be inversely proportional to the sizes  $s_i$  of the sample. In a harmonic trap with trapping frequency  $\omega_i$  along the  $i$  direction one has  $s_i = \sqrt{\frac{k_B T}{m \omega_i^2}}$  where  $k_B$  is Boltzmann's constant and  $T$  is the temperature of the atoms. The parameter  $\eta$  would be unity for a detector whose resolution width  $d$  is small compared to the correlation length. Our  $d$  is smaller than  $l_y$  but larger than  $l_x$  and in this case  $\eta$  is given approximately by  $\frac{l_x}{2d} \sim 5\%$ . We use Eq. 1 to fit the data using  $\eta$  and the  $l_i$  as fit parameters (see Materials and Methods), and compare the results to the ideal gas model.

The results for  $l_x$ ,  $l_y$  and  $l_z$  for our three temperatures are plotted in Figure 3a. The fitted values of  $l_x$  are  $\sim 450 \mu\text{m}$ , and are determined by the detector resolution rather than the true coherence length along  $x$ . The value of  $l_y$  shown in Figure 3a has been corrected for the finite spatial resolution of the detector. The fitted value of  $l_z$  requires no correction since in the vertical direction the resolution of the detector is much better. One sees that  $l_y$  and  $l_z$  are consistent and agree with the prediction using the known trap frequencies and temperatures. In Figure 3b we plot the fitted value of  $\eta$  versus temperature, along with the prediction of the same ideal gas model as in Figure 3a and using the measured detector resolution. The data are in reasonable agreement with the model although we may be seeing too little contrast at the lowest temperature. The run at  $0.55 \mu\text{K}$  was above but very close to the BEC transition temperature. Future work will include examining whether the effect of the repulsive interactions between atoms or finite sample size must be taken into account.

The results reported here show the power of single particle detection in the study of quantum

gases. The correlations we have observed are among the simplest which should be present. Two recent experiments have shown correlations in a Mott insulator (11) as well as in atoms produced from the breakup of molecules near a Feshbach resonance (12). Improved observations of these effects may be possible with individual particle detection. Other atom pair production mechanisms, such as 4-wave mixing (22, 23) can be investigated. A fermionic analog to this experiment using  $^3\text{He}$  would also be (24) of great interest.

## References and Notes

1. R. Hanbury Brown, R. Q. Twiss, *Nature* **177**, 27 (1956).
2. F. T. Arecchi, E. Gatti, A. Sona, *Phys. Lett.* **20**, 27 (1966).
3. R. Glauber, *Phys. Rev. Lett.* **10**, 84 (1963).
4. R. J. Glauber, *Quantum Optics and Electronics*, C. DeWitt, A. Blandin, C. Cohen-Tannoudji, eds. (Gordon and Breach, New York, 1965), p. 63.
5. G. Baym, *Act. Phys. Pol. B* **29**, 1839 (1998).
6. B. Berne, R. Pecora, *Dynamic Light Scattering* (Dover, New York, 2000).
7. U. Fano, *Amer. J. Phys.* **29**, 539 (1961).
8. R. Hanbury Brown, R. Twiss, *Nature* **178**, 1046 (1956).
9. J. S. Bell, *Speakable and unspeakable in quantum mechanics* (Cambridge University Press, Cambridge, 2004), second edn.
10. M. Yasuda, F. Shimizu, *Phys. Rev. Lett.* **77**, 3090 (1996).
11. S. Foelling, *et al.*, *Nature* **434**, 481 (2005).

12. M. Greiner, C. A. Regal, J. T. Stewart, D. S. Jin, *Phys. Rev. Lett.* **94**, 110401 (2005).
13. M. Henny, *et al.*, *Science* **284**, 296 (1999).
14. W. D. Oliver, J. Kim, R. C. Liu, Y. Yamamoto, *Science* **284**, 299 (1999).
15. H. Kiesel, A. Renz, F. Hasselbach, *Nature* **418**, 392 (2002).
16. Y. Kagan, B. V. Svistunov, G. V. Shlyapnikov, *Sov. Phys.–JETP* **42**, 209 (1985).
17. E. A. Burt, *et al.*, *Phys. Rev. Lett.* **79**, 337 (1997).
18. B. Laburthe Tolra, *et al.*, *Phys. Rev. Lett.* **92**, 190401 (2004).
19. A. Robert, *et al.*, *Science* **292**, 461 (2001).
20. O. Jagutzki, *et al.*, *Nucl. Inst. & Meth. in Phys. Res. A* **477**, 244 (2004).
21. M. Naraschewski, R. Glauber, *Phys. Rev. A* **59**, 4595 (1999).
22. L. Deng, *et al.*, *Nature* **398**, 281 (1999).
23. J. Vogels, K. Xu, W. Ketterle, *Phys. Rev. Lett.* **89**, 020401 (2002).
24. R. Stas, J. McNamara, W. Hogervorst, W. Vassen, *Phys. Rev. Lett.* **93**, 053001 (2004).
25. We thank R. Sellem of the DTPI Technology Division, (supported by MRCT-CNRS Federation FR2764, and Université Paris-Sud) for his decisive role in the development of the time-to-digital converter.



**Fig. 1.** Schematic diagram of the apparatus. The MCP has a diameter of 8 cm and is 47 cm below the magnetic trap. The trapped cloud has a cylindrical symmetry with oscillation frequencies  $\omega_x/2\pi = 47$  Hz and  $\omega_y/2\pi = \omega_z/2\pi = 1150$  Hz. During its free fall towards the detector, a thermal cloud acquires a spherical shape. A 1  $\mu$ K temperature yields a cloud with an rms radius of approximately 3 cm at the detector. Single particle detection of the neutral atoms is possible because of the atom's 20 eV internal energy that is released at contact with the MCP. Position sensitivity is obtained through a delay-line anode at the rear side of the MCP. The axes of the trap are at 45° to those of the detector.

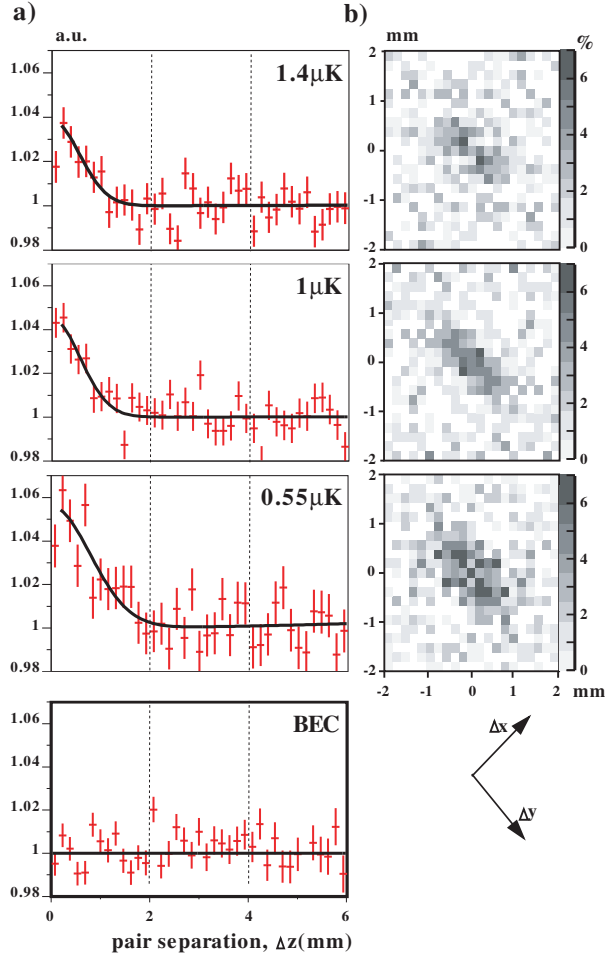


**Fig. 2.** a) Normalized correlation functions along the vertical ( $z$ ) axis for thermal gases at 3 different temperatures and for a BEC. For the thermal clouds, each plot corresponds to the average of a large number of clouds at the same temperature. Error bars correspond to the square root of the number of pairs. b) Normalized correlation functions in the  $\Delta x - \Delta y$  plane for the 3 thermal gas runs. The anisotropy of the initial cloud results in an anisotropic correlation function with inverted ellipticity.

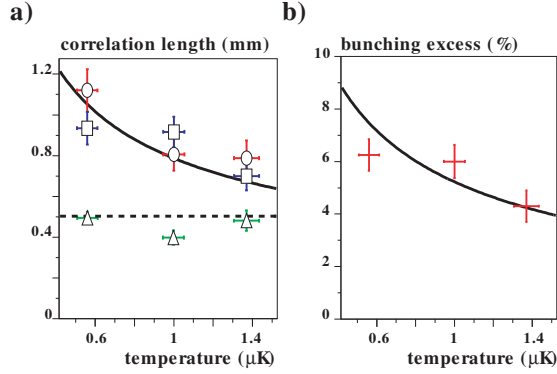


**Fig. 3.** Results of fits to the data in Figures 2a and 2b. a) Fitted correlation lengths  $l_x$ ,  $l_y$  and  $l_z$  along the 3 axes (triangles, squares and circles). Vertical error bars are from the fits. Horizontal error bars correspond to the standard deviation of the measured temperature. Along the  $x$  axis the measurement is entirely limited by the detector resolution. The dotted horizontal line is the result of an independent estimate of the resolution. The result for the  $y$  axis has been corrected for the finite detector resolution as characterized by the fitted value of  $l_x$ . The  $z$ -axis suffers from no such resolution limit. The solid curve corresponds to  $\frac{\hbar t}{ms_z}$  where  $s_z = s_y$  depends on the temperature (see text). b) Fitted contrast  $\eta$  of the correlation function for the three temperatures used. The solid line corresponds to the same non-interacting gas model as the line in a) and includes the finite detector resolution.

## Materials and Methods

**Histogram along  $z$  :** In computing the vertical separation histogram (the unnormalized correlation function), our averaging procedure is as follows. Let the index  $(i, j)$  denote a particular detector pixel in the  $x - y$  plane. We compute the histogram  $h_{i,j}$ , corresponding to vertical separations of the pairs of atoms detected in the pixel  $(i, j)$  as well as the histogram  $h_{i,j;k,l}$ , corresponding to the separations of pairs of atoms one of which was in pixel  $(i, j)$  and the other in pixel  $(k, l)$ . The  $200 \mu\text{m}$  pixel size gives  $\Delta x = (k - i) \times 200 \mu\text{m}$  and  $\Delta y = (l - j) \times 200 \mu\text{m}$ . To improve the signal to noise ratio in the correlation function along the  $z$  axis we form the sum:

$$h_{i,j} + \sum_{a,b} h_{i,j;i+a,j+b} \quad (2)$$

in which  $(a, b) = \{(0, -1), (1, 0), (1, -1), (1, -2), (2, -1), (2, -2), (2, -3), (3, -2), (3, -3)\}$ . The resulting histogram is then summed over all pixels  $(i, j)$  and all the cloud realizations and is plotted in Fig 2a.

The analysis of the BEC presented an additional complication because the high density of the sample, even after expansion, appeared to induce saturation effects in the detector. When observing a BEC with about 1000 detected atoms, the second half of the cloud was detected with much reduced efficiency. This effect was of course more pronounced at the center of the BEC, leading to "banana" shaped rather than circular profiles in the  $y$ - $z$  plane. The saturation effect caused a high sensitivity of the apparent shape of a cloud to the number of atoms in it.

Since our averaging and normalization procedure assume that successive shots have the same temporal shape, the cloud shapes must be corrected before averaging. This correction was done by dividing up each cloud in 8 slices along the  $y$  axis and determining the maximum of the arrival time distribution (recall that the  $z$  axis is the temporal axis). Each segment was

then shifted in time so as to have its maximum coincide with the expected maximum without saturation (308 ms). This procedure produces clouds whose profiles are distorted but whose correlations would be substantially preserved.

**Fitting procedure :** Instead of fitting the data directly to the function  $g_{th}^{(2)}$ , we use a three step procedure, which exploits the Gaussian nature of  $g_{th}^{(2)}$ . First, since our resolution is best along the  $z$  direction, we fit the data of Fig. 2a to  $g_{th}^{(2)}(0, 0, \Delta_z)$  to extract  $l_z$ . The assumption of a Gaussian  $g_{th}^{(2)}$  ensures that the averaging over pixels as described in Eq.2 improves the uncertainty in the fitted value of  $l_z$  only at the cost of a lowered value of  $\eta$ . Then, we fit the normalized experimental correlation function for a given value of  $(\Delta x, \Delta y)$  without the average over pixels in Eq. 2 to  $1 + \eta' \exp[-(\Delta z/l_z)^2]$  and fixing the value of the parameter  $l_z$  to that extracted in the previous step. This gives the value of  $\eta' = \eta \exp(-[(\Delta x/l_x)^2 + (\Delta y/l_y)^2])$  as a function of  $(\Delta x, \Delta y)$  which we plot in Figure 2b. We then fit the data in Figure 2b to  $g_{th}^{(2)}(\Delta x, \Delta y, 0)$  to find  $l_x$  and  $l_y$  and  $\eta$ .

**Electronic detection :** We have also recorded data for a cloud at 1 mK, for which the correlation length is so small that the bunching effect is washed out. Experimentally, the normalized correlation function in this case is indeed flat to within less than 1 %. This ensures that there is no spurious electronic effect on our data.